Journal of
Materials Chemistry A

PAPER

View Article Online
View Journal | View Issue

Cite this: *J. Mater. Chem. A*, 2015, **3**, 18636

A shortcut to garnet-type fast Li-ion conductors for all-solid state batteries†

Semih Afyon,*[a] Frank Krumeich[b] and Jennifer L. M. Rupp*[a]

Ga-doped $Li_7La_3Zr_2O_{12}$ garnet structures are among the most promising electrolytes for all-solid state Li-ion-batteries. The synthesis and processing of garnet-type fast Li-ion conductors depend on conventional sol–gel and solid state syntheses and sintering that are usually done at temperatures above 1050 °C to reach the high Li-ion conducting cubic phase. This process results in micron-sized particles and potential Li-loss, which are unfavorable for further processing and electrode–electrolyte assembly. Here, we tackle this problem and report a novel low temperature synthesis-processing route to stabilize the cubic phase of $Li_7La_3Zr_2O_{12}$, while keeping the nanocrystallites at ∼200–300 nm. $Li_7La_3Zr_2O_{12}$ phases are obtained at temperatures as low as 600 °C by a modified sol–gel combustion method utilizing mainly nitrate precursors, and the sintering temperature is lowered by ∼200 °C compared to the state-of-art. Through a new model experiment, we also shed light on the conditions influencing the tetragonal to cubic phase transformation *via* homogeneous Ga-diffusion and incorporation occurring at a surprisingly low temperature of ∼100 °C for a post-annealing step. The sintered pellets of the newly obtained $Li_{6.4}Ga_{0.2}La_3Zr_2O_{12}$ deliver high bulk Li-ion conductivities in the range of $\sim 4.0 \times 10^{-4}$ S cm^{-1} at 20 °C, and a wide thermal operation window is accessible through its characteristic activation energy of ∼0.32 eV. We report that there is an optimum in sintering-processing conditions for the cubic c-$Li_{6.4}Ga_{0.2}La_3Zr_2O_{12}$ solid state electrolytes and their Li-ionic conductivity and the (Raman) near order characteristics that can be tracked through changes in Li–O vibrational modes. Based on this alternative route, low-temperature synthesized powders can be sintered to relatively dense pellets at around only 950 °C. At higher sintering temperatures (*e.g.* 1100 °C), Li-losses progress as confirmed by structural studies and a reduction of both ceramic pellet density and ionic conductivity, as well as distortions in the Li-sublattice, are found. Through this work, an alternative low temperature processing route for Ga-doped $Li_7La_3Zr_2O_{12}$ garnet type electrolytes for all-solid state batteries is suggested. The new synthesis method and the use of c-$Li_{6.4}Ga_{0.2}La_3Zr_2O_{12}$ nanoparticles could open pathways in terms of preventing Li-loss during the process and advancing future solid electrolyte–electrode assembly options for all-solid state Li-ion batteries.

Received 3rd May 2015
Accepted 2nd August 2015

DOI: 10.1039/c5ta03239c

www.rsc.org/MaterialsA

Published on 04 August 2015. Downloaded by MIT Library on 6/18/2019 3:37:10 PM.

1. Introduction

With their high energy density, long cycle life and variable charge–discharge rates, rechargeable Li-ion batteries are preferred to power electric vehicles by car manufacturers. However, for this most anticipated use of Li-ion batteries, the current technology and electrode materials are still not sufficient to provide cost advantages and high practical energies that could increase the range of electric vehicles, and consequently, enable their large scale use with the elimination of range anxiety experienced by consumers. *Solid inorganic electrolytes* become quite interesting at this point that can enable the use of high capacity electrode materials (*e.g.* sulphur,[1,2] manganese[3–5] and vanadate based cathodes[6–8]), which are otherwise not very stable and safe to be used in liquid organic electrolytes for the current Li-ion battery technology.[9] The use of metallic Li anodes, so further boosting practical energy densities, could also be possible with ceramic electrolytes by preventing the damage of dendritic Li growth. Solid inorganic electrolytes also provide additional advantages such as better thermal and chemical stabilities and the elimination of liquids and separators in electrochemical cells. Here, the development of fast Li-ionic solid electrolyte materials may also be seen as the impetus towards novel types of high power density all-solid state thin film microbatteries[10–12] for electronics[13] or of innovative large scale storage solutions co-operating abundant industrial waste heat to speed up Li-ion diffusion kinetics in solid Li-ion batteries.

---

[a] ETH Zurich, Department of Materials, CH-8093 Zurich, Switzerland. E-mail: jennifer.rupp@mat.ethz.ch; semih.afyon@mat.ethz.ch

[b] ETH Zurich, Department of Chemistry and Applied Biosciences, CH-8093 Zurich, Switzerland

† Electronic supplementary information (ESI) available. See DOI: 10.1039/c5ta03239c

This journal is © The Royal Society of Chemistry 2015

Published on 04 August 2015. Downloaded by MIT Library on 6/18/2019 3:37:10 PM.

Among the solid Li-ionic electrolytes, $Li_7La_3Zr_2O_{12}$ (LLZO) garnets and doped variants revealed the highest Li-ion conductivities in the range of $\sim 10^{-4}$ S cm^{-1} at room temperature,[14,15] as described in the detailed review of Thangadurai's group.[14] High ionic conductivities for $Li_7La_3Zr_2O_{12}$ (LLZO) garnets were first reported by Weppner and co-workers.[16] The crystal structures of the two LLZO polymorphs were later described by Awaka *et al.*[17,18] However, only the cubic phase exhibits superior Li-ion conductivity close to the classic liquid Li-ion electrolytes; its stabilization over the lower conducting tetragonal phase and the management of Li-losses relative to sintering conditions remain challenging. Though initial studies suggested a high temperature stabilization of the high Li-ion conducting cubic phase, recent reports showed that the stabilization of the cubic phase mostly depends on the formation of disordered and partially occupied Li-sites and vacancies that cannot be obtained without a stabilizing agent;[19–21] *vice versa* either full or empty Li sites exist for the low-conductive tetragonal phase. Currently, there is much debate surrounding the best stabilization strategy for the desired cubic LLZO phase. For example, the high temperature stabilization reported in some investigations could be linked to either intentional or unintentional doping of Al^{3+} as present in reaction crucibles during the sintering of ceramics. When Al^{3+} is doped into LLZO, additional charge compensation takes place through emergence of Li^+-vacancies which reduce the free energy associated with ordering of the Li-sublattice, eventually leading to cubic symmetry change with disordered partially occupied Li-sites.[19,21] It is to be noted that only minor concentrations of Al in LLZO (*ca.* 0.10–0.15 Al per formula unit of LLZO)[22,23] are required to stabilize the cubic LLZO phase. In addition, Li loss for sintering at high temperatures (*i.e.* for >1000 °C) and the material's protonic exchange of H^+/Li^+ in humidified air are also discussed to facilitate the phase transition to cubic LLZO.[24] The significance of stabilizing the cubic phase for LLZO ceramics can directly be demonstrated in the two orders of magnitude divergence of Li-ion conduction reported for $Li_{7-3x}(Al_x)La_3Zr_2O_{12}$ ($x = 0$ to 0.5), $\sim 10^{-6}$ to 10^{-4} S cm^{-1} at ambient conditions, being dependent on the degree of structural Li-site occupancy, disorder, relative density and microstructure of the pellets.[21–23,25,26] Thus, Al^{3+} doping into LLZO has been adopted as a key route to obtain the high Li-ion conducting cubic phase. In addition to Li-site doping, the partial substitution of Zr^{4+} with a metal ion of a different oxidation state has also been extensively investigated to improve the Li-ion conductivity *via* the formation of additional vacancies.[27–29]

Very recently, the stabilization of the cubic phase has been demonstrated by an alternative strategy through Ga^{3+} substitution of Li^+,[30–33] instead of Al^{3+}, which isn't surprising considering the similar oxidation states and ionic radii of Al^{3+} and Ga^{3+} at tetrahedral coordination sites for a cubic LLZO structure type. Wolfenstine *et al.* showed an ionic conductivity of 3.5×10^{-4} S cm^{-1} for a hot pressed pellet of $Li_{6.25}Ga_{0.25}La_3Zr_2O_{12}$ with 91% relative density.[31] Shinawi and Janek stabilized the cubic phase for a series of Ga:LLZO compounds and revealed optimized Li-ion conductivity (5.4×10^{-4} S cm^{-1}) for a 92.5% dense pellet of 1.0 mol% Ga LLZO obtained through conventional isostatic pressing and sintering.[32] Excitingly, the microstructural locality of excess Ga incorporation in the ceramics was discussed, wherein a clear proof for $LiGaO_2$ acting also as a sintering aid at grain boundaries easing Li-diffusion was identified.[32] The Slater group confirmed through ^{71}Ga NMR the increased ionic conductivity of 1.0×10^{-4} S cm^{-1} to be related to Ga^{3+} incorporation on tetrahedral lattice sites stabilizing cubic LLZO.[30] Moreover, the detrimental effect of humidity on ionic conductivity was also demonstrated in their study. Rettenwander *et al.* also investigated a series of Ga-doped LLZO compounds in detail and gave insights on the crystallographic position of Ga^{3+} through ^{71}Ga Magic Angle Spinning (MAS) NMR spectroscopy at high magnetic fields.[34,35] In their recent study, they revealed that Ga^{3+} can occupy both the 24d and 96h sites in $Li_{7-3(x+y)}Ga_xAl_yLa_3Zr_2O_{12}$ garnets that is different from previous studies showing a single site residence for Ga^{3+}.[35] Furthermore, Kilner and co-workers gave clear guidance on how to increase the pellet densities, up to 94%, for a series of Ga-substituted garnet pellets by sintering in an O_2 atmosphere and improved ionic conductivities to the proximity of 10^{-3} S cm^{-1}.[33] However, despite the technological promise of LLZO compounds as fast conducting Li-electrolytes, there is a subtle balance to be matched between high sintering temperatures required to assure the stabilization of the cubic phase at high density on the one hand, and minimizing Li-losses from the system at these high temperatures on the other. Conventionally, the processing of these ceramics is based on either sol–gel or solid state syntheses of the powder constituents, and the sintering is usually restricted to temperatures above 1050 °C to ensure formation of the high Li-ion conducting cubic phase.[14] The high temperature synthesis also produces micron-sized particles, which are unfavorable for further processing and electrode–electrolyte assembly. Though few reports[36–38] on synthesis methods for cubic-LLZO nanoparticle processing utilizing a low temperature of 750 °C exist, usually low theoretical densities around 60% with unfavorable ionic conductivities in the range of 10^{-6} S cm^{-1} were demonstrated.[37,38] In principle, it is to be noted that all-solid state Li-batteries do not necessarily require fully dense ceramic electrolytes, as long as the throughput Li-ionic transfer is maximized in the bulk electrolyte to an acceptable range around 10^{-4} S cm^{-1} and allows for fast electrode–electrolyte interface transfer kinetics with high mechanical interface stability. Hence, potential reduction of the processing temperature and new nano-particle processing routes to stabilize the highly desired fast conducting Li-garnet phases would enable new ways for battery cell assembly and a wider choice of high capacity electrodes in view of their stability. For example in all-solid state Li-batteries, the utilization of LLZO nano-particles will be very advantageous in any future low-temperature co-sintering route to assemble stable solid electrode–electrolyte interfaces with fast Li diffusion kinetics and has the potential to maximize the electrode surface area or even be the base of a composite electrode. But, this aspect of garnet-type fast Li-ion conductors is not yet optimized and requires new alternative approaches for low-temperature processing of Ga:LLZO nanoparticle and ceramic pellets to fundamentally study the interplay of structure and phase evolvement *vs.* Li-ion diffusion.

Published on 04 August 2015. Downloaded by MIT Library on 6/18/2019 3:37:10 PM.

In this work, we report a *novel low temperature synthesis-processing route* for cubic $Li_{6.4}Ga_{0.2}La_3Zr_2O_{12}$ through which the synthesis-sintering temperature is decreased by ~200 °C compared to the state-of-art, *viz.* nano-particles of the compounds are obtained at a temperature as low as 600 °C by a modified sol–gel combustion method utilizing mainly nitrate precursors. We demonstrate in model experiments that the tetragonal to cubic LLZO phase transformation can occur at a very low temperature of 100 °C by post-synthetic Ga-doping of originally tetragonal nano-powders. Only low thermal activation is required to incorporate Ga^{3+} into the Li-garnet structures. A basic model of the chemical and microstructural evolution from the nano-particle formation to dense sintered pellets of submicron grain size which can be used for all-solid state battery electrolytes is presented. High Li-ion conductivities in the range of more than 10^{-4} S cm^{-1} at room temperature are reached for the low temperature synthesized c-$Li_{6.4}Ga_{0.2}La_3Zr_2O_{12}$. Comparable Li-ion conductivities are usually obtainable through more laborious and not easily accessible techniques-methods (*e.g.* hot press, special protective atmospheres, *etc.*) at higher processing temperatures. To gain deeper insights, we further investigate the Li-ionic conductivity and structural changes *vs.* sintering processing temperature to study the correlation and implicate on the best processing strategy to avoid Li-losses. The new synthesis route and the utilization of nano-c-$Li_{6.4}Ga_{0.2}La_3Zr_2O_{12}$ could open new pathways in terms of a simplified solid electrolyte–electrode assembly and the prevention of Li-loss during synthesis and processing due to the strongly lowered temperatures and high sintering activity.

2. Experimental section

2.1 Synthesis

Stable sols are obtained by dissolving stoichiometric amounts of $LiNO_3$ (99.99%, Merck), $La(NO_3)_3\cdot(H_2O)_6$ (99.9%, Alfa Aesar), and zirconium(IV) 2,4-pentanedionate (Alfa Aesar) in a water and ethanol mixture. Importantly, water and ethanol dissolve nitrate and pentanedionate compounds, respectively. After the salts are completely dissolved, a gel powder is obtained by evaporating the solvent at 90 °C. Firing of the gel-powder at ~600–650 °C for 1 to 10 hours in alumina crucibles with lids placed in a muffle furnace yields the tetragonal phase t-$Li_7La_3Zr_2O_{12}$. The tetragonal phase, t-$Li_7La_3Zr_2O_{12}$, can be obtained at a temperature as low as 600 °C and for an annealing time of 1 hour, but to ensure a high purity phase, a heating profile at 650 °C for 10–15 hours is usually applied. To obtain the cubic phase of $Li_7La_3Zr_2O_{12}$, stoichiometric amounts of Ga_2O_3 and t-$Li_7La_3Zr_2O_{12}$ that would give a composition of $Li_{6.4}Ga_{0.2}La_3Zr_2O_{12}$ are thoroughly mixed in an agate mortar. Annealing the Ga_2O_3 + t-$Li_7La_3Zr_2O_{12}$ mixture at ~600–650 °C, either in the powder form or as pressed pellets covered with the parent powder for 10 hours, yields the cubic phase c-$Li_{6.4}Ga_{0.2}La_3Zr_2O_{12}$ with small nanoparticle sizes of ~200–300 nm. The synthesis procedure is also summarized in Fig. 1a.

Throughout the study, all sample powders are kept under an inert atmosphere (*e.g.* Ar) after the synthesis to minimize the exposure to humidity. Though no major Li-loss is expected due to the low annealing temperature, still the Li-precursor ($LiNO_3$) is taken in a slightly excess amount of 1–2 mol% for the synthesis.

2.2 Characterization

A STOE Stadi P diffractometer equipped with a germanium monochromator and $CuK_{\alpha1}$ radiation (operated at 35 mA, 35 kV) was used to acquire powder X-ray diffraction patterns of the samples. Dilatometry curves were recorded with a TA Instruments DIL 806 optical dilatometer. Scanning electron microscopy (SEM) analysis of the samples was carried out with a Zeiss Gemini 1530 operated at 5 kV. For (scanning) transmission electron microscopy ((S)TEM) analysis the material was deposited on a carbon foil supported on a Cu grid. TEM was performed on a Tecnai F30 microscope (FEI; field emission gun) operated at 300 kV (point resolution ~ 2 Å), STEM and energy-dispersive X-ray spectroscopy (EDXS) on a Hitachi HD 2700 CS microscope equipped with an EDX spectrometer (EDAX). Raman spectroscopy was carried out with a confocal WITec CRM200 Raman microscope instrument (WITec, Germany) equipped with a 532 nm wavelength laser for excitation, and the spectral resolution was 0.7 cm^{-1}.

2.3 Electrochemical tests

For AC electrochemical impedance studies, c-$Li_{6.4}Ga_{0.2}La_3Zr_2O_{12}$ pellets were processed from Ga_2O_3 + t-$Li_7La_3Zr_2O_{12}$ mixtures and symmetric electrodes were applied. Stoichiometric amounts of Ga_2O_3 and freshly synthesized t-$Li_7La_3Zr_2O_{12}$ were thoroughly mixed in an agate mortar and pressed into pellets with a uniaxial press at 35 kN. The pellets obtained this way were further processed in an isostatic press at a pressure of 1000 kN and sintered at 950 °C for 6 hours covered with the parent powder to avoid Li-losses and Al contamination from the alumina crucibles. The resulting pellets usually have a thickness of roughly 1 mm and a diameter of ~9–10 mm, respectively.

Pt was sputtered on both sides of the pellets (BAL-TEC, SCD 050 Sputter-Coater) and Pt wires were sandwiched between two layers of Pt paste (Heraeus C 3605 S) using ceramic binders (Roth, Thermokitt (A) & (B)) to ensure best contacts, see Fig. 5a. Pellet drying after the application of pastes and binders was done under vacuum to protect the pellets from humidity.

Electrochemical impedance spectra were measured with a Gamry Reference 600 potentiostat/galvanostat/ZRA within a range of 1 MHz to 1 Hz. The spectra were characterized using the ZView software.[39] Cable and wiring resistances in the measurement system were approximated to 3 Ω based on a constant value for high temperature measurements. High temperature measurements (>100 °C) were performed under dry synthetic air to avoid humidity exposure. For this, symmetric Pt–LLZO–Pt (electrode–electrolyte–electrode structures) were introduced in an own-constructed atmospheric-closed tube furnace (20–1100 °C) equipped with electrical and gas flow connections and a sample test platform for which temperature values and gradients were recorded exactly next to the sample by K-type thermocouples.

This journal is © The Royal Society of Chemistry 2015

Published on 04 August 2015. Downloaded by MIT Library on 6/18/2019 3:37:10 PM.

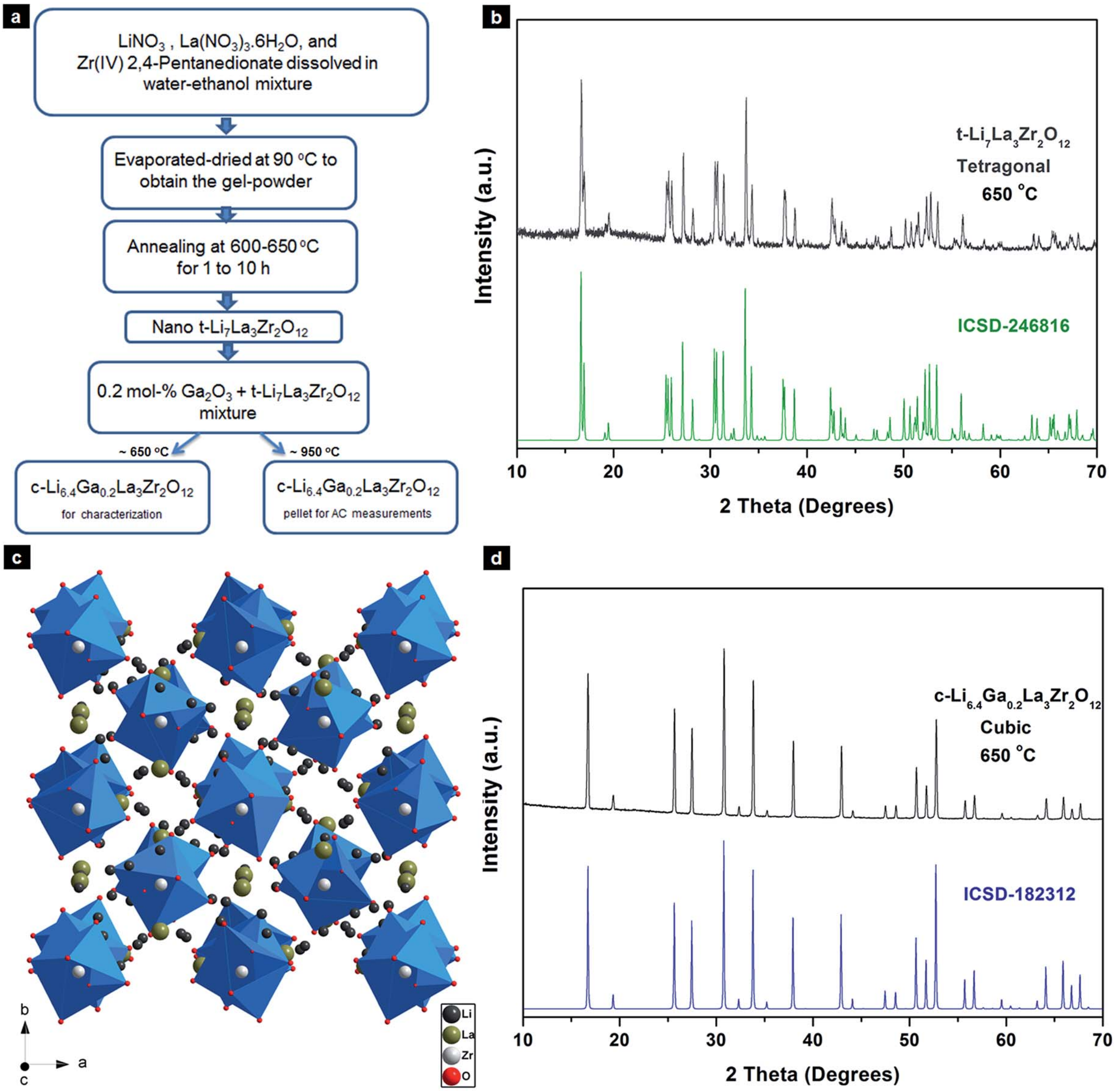

Fig. 1 (a) Scheme for the modified sol–gel combustion synthesis and model experiment to stabilize the fast Li^+ conducting cubic phase through post-Ga_2O_3 addition to the tetragonal phase. (b) XRD powder patterns of t-$Li_7La_3Zr_2O_{12}$ (calculated (green) and experimental (black)). (c) Cubic c-$Li_7La_3Zr_2O_{12}$ (LLZO) garnet structure displayed along skew [001]. (d) XRD powder patterns of c-$Li_{6.4}Ga_{0.2}La_3Zr_2O_{12}$ (calculated (blue) and experimental (black)).

3. Results and discussion

3.1 Novel low temperature synthesis-processing route for t-$Li_7La_3Zr_2O_{12}$ and c-$Li_{6.4}Ga_{0.2}La_3Zr_2O_{12}$ solid state Li-ion electrolytes

Wet chemistry routes ensure a more homogeneous mixing of precursors compared to solid state synthesis methods. This also facilitates the synthesis of single phase products at lower temperatures. This way, the utilization of nitrate salt precursors and firing the gel-powder obtained from them have also been demonstrated to yield various Li-compounds such as $Li_2FeP_2O_7$,[40] $LiMnBO_3$,[41] and $LiCoBO_3$ [42] at much lowered temperatures.[40–42] Exothermic combustion reactions are suggested as the driving force for the formation of those phases at lowered temperatures. Herein, similarly, we show a novel low temperature combustion method to produce LLZO solid electrolytes, whereby in a first step tetragonal $Li_7La_3Zr_2O_{12}$ is obtained and eventually transfered to the cubic phase through post-Ga_2O_3 additions and low-temperature treatment, as shown in the scheme Fig. 1a. Interestingly, the synthesis route suggested is also a model experiment to fundamentally investigate the role of Ga-structural incorporation and diffusion, and their implication on cubic phase transition in garnets, since the tetragonal $Li_7La_3Zr_2O_{12}$ is already formed in the first synthesis step.

Different from the aforementioned syntheses for cathode materials[40–42] and other sol–gel syntheses reported for LLZO,[33,43] we use no carboxylic acids (*e.g.* citric acid) and ethylene glycol during the synthesis. These compounds are mainly used as

Published on 04 August 2015. Downloaded by MIT Library on 6/18/2019 3:37:10 PM.

complexing agents and solvents, and in the case of cathode materials, they provide additional advantages like a reducing atmosphere (*e.g.* CO, through decomposition during calcination) maintaining the desired low oxidation states for transition metals (*e.g.* Fe^{2+}, Co^{2+}, Mn^{2+}) and also giving fine conductive carbon coatings on particle surfaces at the end. However, these are unwanted properties for the synthesis of LLZO powders, so that they are compensated through special measures, such as longer annealing times and higher calcination temperatures to completely burn off organic residues or annealing under an O_2 atmosphere, and these processes produce unfavorable large micron-sized particles.

Our synthesis yields the desired tetragonal phase of small-grained and pure t-$Li_7La_3Zr_2O_{12}$ powder after the first reaction-step at 600–650 °C for 1 to 10 h: the XRD powder pattern of tetragonal t-$Li_7La_3Zr_2O_{12}$ is shown in Fig. 1b. The product has a

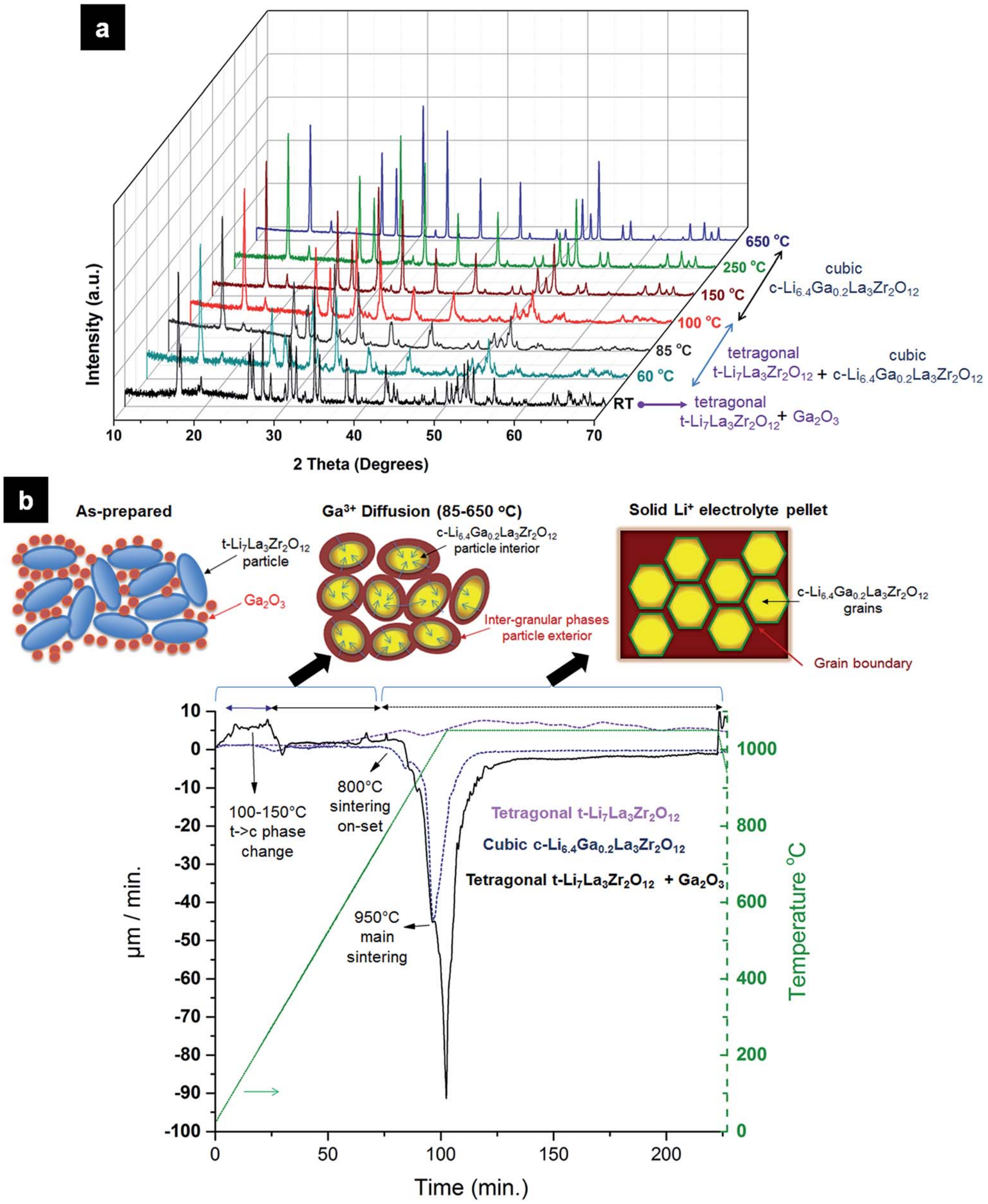

Fig. 2 (a) *In situ* heated XRD powder patterns to study in a model experiment the incorporation of post-added Ga_2O_3 to originally t-$Li_7La_3Zr_2O_{12}$ and phase change with respect to temperature (5 °C min^{-1} heating rate and annealing 15 minutes at each temperature). The desired fast conducting cubic phase evolves already at a temperature as low as 85 °C for the post-Ga_2O_3 addition route, indicating the fast and low-temperature diffusion kinetics of Ga^{3+} ions to the garnet structure. (b) Differential dilatometry plots with a constant heating rate of 10 °C min^{-1} for t-$Li_7La_3Zr_2O_{12}$ + Ga_2O_3 (black), c-$Li_{6.4}Ga_{0.2}La_3Zr_2O_{12}$ (blue), and t-$Li_7La_3Zr_2O_{12}$ (purple). Peaks display the phase transformation, onset and main characteristics of the sintering for t-$Li_7La_3Zr_2O_{12}$ + Ga_2O_3 (black). In comparison, proving the effect of post-Ga doping, no phase transformation peaks can be observed for c-$Li_{6.4}Ga_{0.2}La_3Zr_2O_{12}$ (blue), and for t-$Li_7La_3Zr_2O_{12}$ (purple). In addition, the tetragonal phase of t-$Li_7La_3Zr_2O_{12}$ (purple) displays no sintering and densification at all within the same test conditions. In accordance with the sintering characteristics and *in situ* XRD analysis, we indicate schematic drawings highlighting a model for Ga^{3+} diffusion and its role in stabilizing the cubic phase in the low temperature synthesis of the initial particles and on sintering to dense electrolyte pellets.

This journal is © The Royal Society of Chemistry 2015

Published on 04 August 2015. Downloaded by MIT Library on 6/18/2019 3:37:10 PM.

high purity and the diffraction peaks can be matched with the theoretical pattern (ICSD 246816 [17]). The presence of the slightly broadened diffraction peaks displays the low dimensional character of the t-$Li_7La_3Zr_2O_{12}$ crystallites. In order to reach the high Li-conducting cubic phase and also to fundamentally investigate the role of Ga^{3+} incorporation in structural phase change starting from the tetragonal phase, we applied in the next step of the synthesis post-synthetic Ga-doping. For this, stoichiometric amounts of Ga_2O_3 and t-$Li_7La_3Zr_2O_{12}$ that would result in a composition of $Li_{6.4}Ga_{0.2}La_3Zr_2O_{12}$ (given the substitution of Ga^{3+} with $3Li^+$) are thoroughly mixed in an agate mortar and post-annealed at ~600–650 °C for 10 hours. Fig. 1d represents the XRD powder pattern of c-$Li_{6.4}Ga_{0.2}La_3Zr_2O_{12}$. All diffraction peaks of the synthesized powder are associated with the cubic phase of LLZO (ICSD 182312 [18]), and they can be indexed using Werner's algorithm (TREOR)[44] (Table S1†) with a cubic cell constant of 12.974(4) Å. Accordingly, the reported cubic LLZO structure[16,18] is presented in Fig. 1c. The cubic $Li_7La_3Zr_2O_{12}$ crystallizes in $Ia\bar{3}d$, where La^{3+} (Wyckoff position 24c) and Zr^{4+} (Wyckoff position 16a) are dodecahedrally and octahedrally coordinated by oxygen neighbors. Li^+ ions are in tetrahedral coordination and fractionally occupy two different sites (Wyckoff positions 24d and 96h). According to the previous investigations with ^{71}Ga NMR and neutron diffraction,[30,33] Ga^{3+} is expected to substitute $3Li^+$ ions in the Li-ion sublattice and stabilize the cubic structure. 3D Li-diffusion pathways made by closely spaced, disordered and vacant Li sites provide high Li-ion conductivities for the cubic LLZO. In order to confirm the influence of post-synthetic Ga-doping, the calcined powders are also re-annealed at 650 °C without adding any Ga_2O_3, and in this case, the samples still remain in the tetragonal phase, see ESI Fig. S1.† Moreover, syntheses performed with post-synthetic Ga-doping in glassy carbon crucibles rather than alumina crucibles still yield the cubic phase of LLZO, eliminating any role of Al^{3+} incorporation in the phase transformation observed here, see ESI Fig. S2.† Therefore, we clearly demonstrate the influence of post-synthetic Ga-doping and Ga^{3+} incorporation into the structure.

3.2 Ga-diffusion and incorporation into low temperature synthesized t-$Li_7La_3Zr_2O_{12}$ and microstructure analysis for c-$Li_{6.4}Ga_{0.2}La_3Zr_2O_{12}$: a model experiment

To reveal more insights about the phase transformation and the effect of post-synthetic Ga_2O_3 addition, a series of XRD patterns

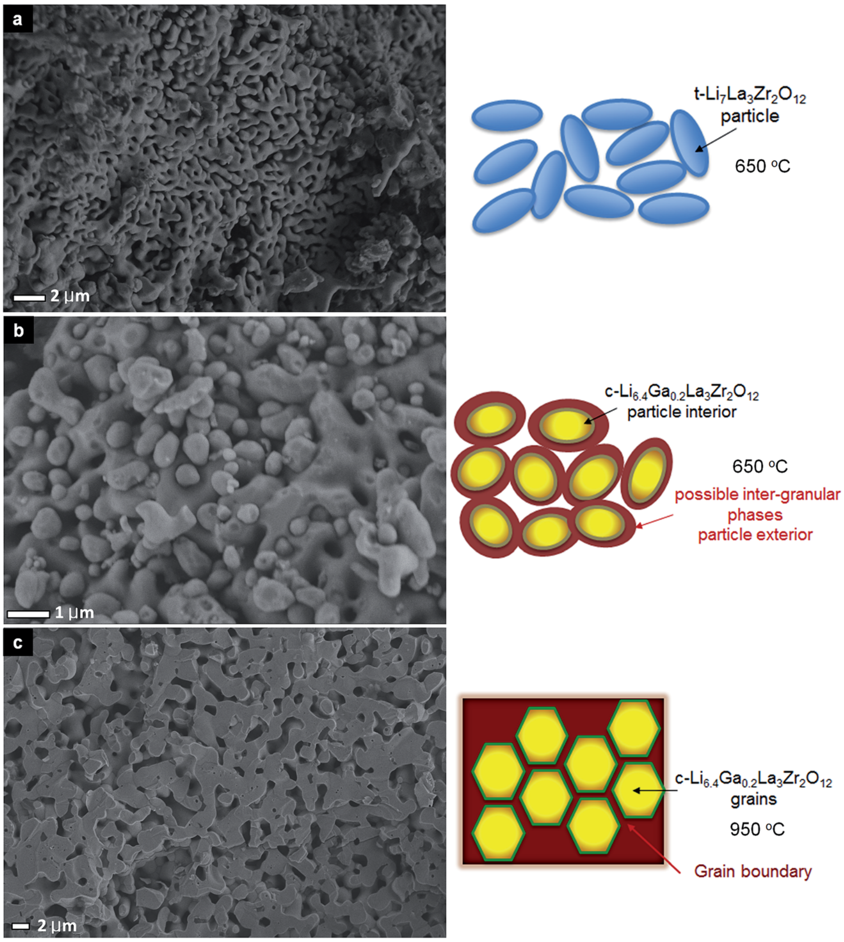

Fig. 3 Scanning electron microscopy (SEM) images of (a) tetragonal t-$Li_7La_3Zr_2O_{12}$ powder, (b) c-$Li_{6.4}Ga_{0.2}La_3Zr_2O_{12}$ powder, and (c) a pellet cross-section of c-$Li_{6.4}Ga_{0.2}La_3Zr_2O_{12}$. Schematics for the microstructures based on SEM and also in view of the *in situ* heating XRDs and dilatometry to study the microstructural evolution and Ga uptake to the Li-garnet structures are presented.

Published on 04 August 2015. Downloaded by MIT Library on 6/18/2019 3:37:10 PM.

were recorded for *in situ* heated Ga_2O_3 + t-$Li_7La_3Zr_2O_{12}$ powders with respect to the post-annealing temperature, see Fig. 2a; here, again, the ratio was fixed at 0.2 Ga per formula unit of t-$Li_7La_3Zr_2O_{12}$. We observe a phase transition starting at ∼85 °C, and a single cubic c-$Li_{6.4}Ga_{0.2}La_3Zr_2O_{12}$ phase is measurable already at a temperature as low as ∼150 °C. This is also a model experiment highlighting Ga-diffusion to particles that cannot be directly compared with other previous studies, as conventionally Ga is already added to the LLZO directly in the first solid state or sol–gel syntheses.[30–33] Through Ga diffusion to the tetragonal phase upon heating, as sketched in Fig. 2b, the Ga-doped cubic LLZO phase forms according to the present XRD results in the bulk of the particles. Ga diffusion into oxides at such low temperatures was also observed by Mikkelsen *et al.*[45]

To further identify the impact of Ga-diffusion into the t-$Li_7La_3Zr_2O_{12}$ particles on their phase change and sintering characteristics, we turn to dilatometry measurements on pressed ceramic powder green bodies and correlate the observed changes with diffraction results in the given schematics showing the phase evolution and densification over time. Firstly, in agreement with the *in situ* XRD studies, the dilatometry measurements confirm the phase transformation at around ∼100 °C shown by a starting volume expansion (broad peak at differential dilatometry plots and expansion in relative dilatometry curves at ∼100 °C), see Fig. 2b and ESI Fig. S3.† In contrast, such volume changes are neither present for the reference green pellet of t-$Li_7La_3Zr_2O_{12}$ without Ga-addition nor for the already transformed green pellets of cubic $Li_{6.4}Ga_{0.2}La_3Zr_2O_{12}$ (already annealed-transformed powder mixture at ∼600–650 °C for 10 hours, then pressed into green pellets), see Fig. 2b. As the cubic LLZO unit cell has a larger volume than the tetragonal LLZO cell,[17,18] the observed volume expansion fits well with the expectation upon phase transformation. But, it should be noted that the pellet geometry could slightly change upon phase transformation, so that the volume change values deduced from the dilatometry curves should not be evaluated as quantitative values reflecting the exact volume change at the unit cell level. Secondly, the onset temperature and the main sintering temperature for c-$Li_{6.4}Ga_{0.2}La_3Zr_2O_{12}$ pellets are also found to be ∼800 °C and ∼950–975 °C, respectively, Fig. 2b. In comparison with the previous reports on cubic LLZO,[25,26,46] the onset sintering temperature is lowered by ∼300 °C, and the effective sintering temperature to reach a relative density above 75% is decreased by ∼200 °C. The densification at a lower sintering temperature is attributed to the large specific surface area of the nano-grained material resulting in better contact between the crystallites. As a consequence, this promotes grain boundary and volume diffusion which is further supported by Ga acting as a sintering agent[32] at the grain boundary. Excitingly, the nature of the model experiment demonstrates that before sintering is even active, Ga^{3+} is already incorporated into the LLZO structure and induces phase transformation to the desired cubic phase at temperatures as low as 100 °C, even long before an active grain boundary has formed in the green bodies. The phase transformation at such low temperatures was also observed by Larraz *et al.*, however, in that case, the material's protonic exchange of H^+/Li^+ in humidified air was shown to induce the phase transition to cubic LLZO.[24] But, here, we clearly demonstrate that the transformation was caused by post-synthetic Ga doping, as t-$Li_7La_3Zr_2O_{12}$ samples without Ga-addition do not show any sign of phase change (see ESI Fig. S1, S3† and 2b).

Scanning electron microscopy (SEM) micrographs of t-$Li_7La_3Zr_2O_{12}$ and c-$Li_{6.4}Ga_{0.2}La_3Zr_2O_{12}$ powders and sintered pellets are displayed in Fig. 3. Transmission electron microscopy (TEM) images for t-$Li_7La_3Zr_2O_{12}$ and c-$Li_{6.4}Ga_{0.2}La_3Zr_2O_{12}$ powders are shown in ESI Fig. S4.† For tetragonal t-$Li_7La_3Zr_2O_{12}$, the shape of the particles is not very well-defined and the crystallite size of t-$Li_7La_3Zr_2O_{12}$ particles approximately ranges from 300 nm to 1 μm after the synthesis at 650 °C, see Fig. 3a and ESI Fig. S4.† The smaller crystallites also form agglomerates in the range of 2 to 10 microns. With the phase transformation to the cubic phase, it can be observed that spherical nano-crystallites of c-$Li_{6.4}Ga_{0.2}La_3Zr_2O_{12}$ emerge from the larger particle agglomerates, see Fig. 3b. The nano-crystallites of c-$Li_{6.4}Ga_{0.2}La_3Zr_2O_{12}$ are mostly in the range of ∼200–300 nm, see Fig. 3b and ESI Fig. S4,† which is one of the smallest reported for garnet-type fast Li-ion conductors compared to the literature.[22,26,29,32] The SEM image of a c-$Li_{6.4}Ga_{0.2}La_3Zr_2O_{12}$ pellet cross-sectional surface after sintering to 950 °C for 6 hours is shown in Fig. 3c. It is clearly visible that densification of the sample and good inter-grain connectivity are achieved in agreement with the sintering characteristics. No clearly distinct large grains in the micron regime can be observed in SEM micrographs and an isotropic shape is found for the cubic $Li_{6.4}Ga_{0.2}La_3Zr_2O_{12}$ sintered pellets. The grain boundaries show no sharp fringes and appear as a potential glass-like inter-granular phase. Our findings may suggest that for the given novel low temperature processing route one may observe such glass-like inter-granular Ga-rich phases also at lower Ga-doping concentrations and for smaller average grain sizes of the sintered ceramics. Thus, we demonstrate through the new synthesis route, in comparison with previous solid state synthesized powders and sintered pellets, that the $Li_{6.4}Ga_{0.2}La_3Zr_2O_{12}$ pellets reported here reveal considerably lowered mean grain sizes for comparable sintering conditions and Ga-doping.[31,32]

Motivated by the microstructural finding, we turn to scanning transmission electron microscopy (STEM) to elucidate the nature of gallium incorporation and distribution in our post-synthetic Ga-doped LLZO synthesized at 650 °C. Previously, it was shown that Ga^{3+} substitutes Li^+ in tetrahedral sites leading to the stabilization of the cubic phase *via* the formation of disordered Li-sites and vacancies;[30,33] however, the presence of Ga in grain boundaries as $LiGaO_2$, rather than going into the garnet structure, was also reported by El Shinawi and Janek for 0.3 to 1.0 mol Ga doped LLZO.[32] Here, we found a homogeneous Ga distribution in the nanoparticles of cubic c-$Li_{6.4}Ga_{0.2}La_3Zr_2O_{12}$, see Fig. 4. In addition, also, Zr and La distributions are homogeneous over the investigated nano-particles. SEM-EDXS analysis performed at the c-$Li_{6.4}Ga_{0.2}La_3Zr_2O_{12}$ pellet cross-sectional surface after sintering to 950 °C for 6 hours also confirms the homogeneous distribution of elements, and in addition, elemental ratios for Ga, La and Zr are found to be in close proximity to the initial composition (see ESI Fig. S5†).

This journal is © The Royal Society of Chemistry 2015

Published on 04 August 2015. Downloaded by MIT Library on 6/18/2019 3:37:10 PM.

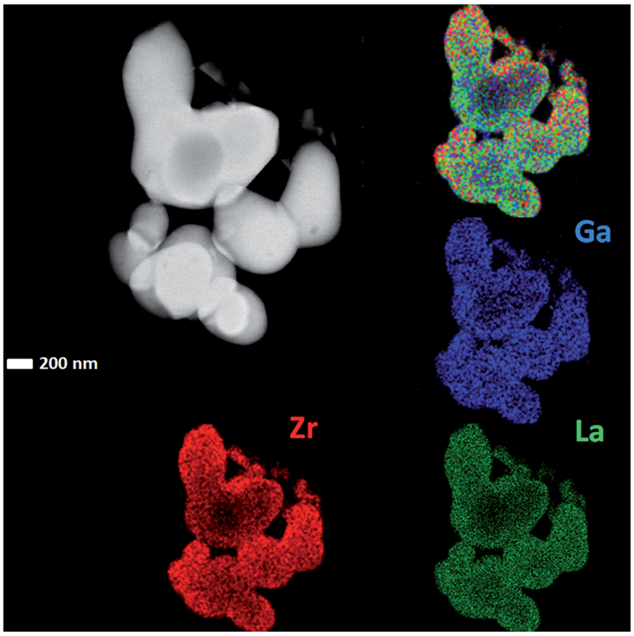

Fig. 4 Scanning transmission electron microscopy (STEM) images and elemental mapping of cubic c-$Li_{6.4}Ga_{0.2}La_3Zr_2O_{12}$ powders (synthesized at 650 °C) are presented. The homogeneous distribution of Zr (red), La (green) and Ga (blue) are shown for their superposition and single mapping over the nanoparticles. No enrichment either in the bulk grain cores or towards the grain boundary-close interfaces is measurable within the limit of STEM and elemental mapping carried out.

Besides, within the detection limit of the technique, EDX spectra obtained from the selected regions in cross-sectional images do not show any major Al contamination that might result from the alumina crucibles used during the sintering of pellets (see ESI Fig. S6†).

Any enrichment of Ga in grain boundaries cannot be observed, so it can be predicted that Ga^{3+} predominantly goes into the garnet structure substituting Li^+ in a similar way to the former discussed reports.[30,33] However, in agreement with the findings from dilatometry characteristics, cross-sectional SEM micrographs and the investigations of Janek *et al.*, possible glass-like inter-granular Ga-rich phases acting as sintering agents can also be suggested. The existence of such amorphous inter-granular phases is found in some regions through our TEM investigations, where the amorphous nano-particles with a lack of order even at 20 nm resolution can be observed (see ESI Fig. S7†). It may be hypothesized that the amorphous inter-granular phase consists of Ga_2O_3, Li-compounds (*e.g.* Li_2O, Li_2CO_3) that could eventually form in air starting from the exchange of Li^+ in the LLZO structure with Ga^{3+}, $LiGaO_2$ and other glassy Ga and Li rich materials.

3.3 Lithium ionic conductivity, sintering characteristics and Raman near order characteristics of low temperature synthesized c-$Li_{6.4}Ga_{0.2}La_3Zr_2O_{12}$ electrolyte pellets

The ionic conductivity of the low temperature synthesized cubic c-$Li_{6.4}Ga_{0.2}La_3Zr_2O_{12}$ was examined by AC electrochemical impedance spectroscopy using Pt electrodes, Fig. 5. For this, the sintering temperature of the pellet (processed from Ga_2O_3 + t-$Li_7La_3Zr_2O_{12}$ mixture) is chosen based on the dilatometry profiles, where the main shrinkage for the pellet occurs at ~950 °C (accordingly we employ an isothermal hold for 6 hours, 5 °C min^{-1} heating rate), Fig. 2b. After the sintering process, pellets usually have relative densities in the range of ~76–80%. The relative density was calculated through the processed pellet's mass and volume (geometrically derived).

A typical Nyquist plot of c-$Li_{6.4}Ga_{0.2}La_3Zr_2O_{12}$, measured at RT in air, is displayed in Fig. 5b. The main characteristics of the impedance spectrum are a resistance off-set at high frequencies, a compressed semicircle at intermediate frequencies, and a tail at low frequencies. The impedance data were fitted with an equivalent circuit of $(R_{\text{bulk}})(R_{\text{gb}}Q_{\text{gb}})(Q_{\text{electrode}})$, R denotes the resistance and Q the constant phase element contributions of the respective bulk (R_{bulk}), grain-boundary (R_{gb}), and electrode contributions. We ascribe the low frequency constant phase element, $Q_{\text{electrode}}$, to the electrode–electrolyte (Pt–LLZO) interfaces due to their variation upon opposed test bias (over potentials). The higher frequency intercept and the compressed semicircle can be attributed to bulk and grain-boundary contributions and agree well with earlier reports.[29,30] Notably, ionic conductivities of 4.0×10^{-4} S cm^{-1} (bulk) and 0.24×10^{-4} S cm^{-1} (total) are determined for the low temperature synthesized cubic c-$Li_{6.4}Ga_{0.2}La_3Zr_2O_{12}$ at ambient conditions, Fig. 5. The employment of nano-particles might be considered to lead to an increase in total resistance due to the formation of additional grain boundaries. But this is not the case here, as the total ionic conductivity (R_{bulk} + R_{gb}) obtained here is still considerably high with the good inter-grain connectivity provided through the successful sintering of nano-particles and glass-like inter-granular phase. The Arrhenius activation of bulk Li ionic conductivity is displayed in Fig. 5c. The activation energy of conductivity is ~0.32 eV being in good agreement with previous studies.[14] It can also be observed that the bulk contribution in the impedance spectra becomes more apparent with an incomplete semicircle for the higher resistive pellets, which are intentionally exposed to air for longer periods of time, see ESI Fig. S8 and S9.† The resistance values further increase as the exposure of pellets are prolonged (ESI Fig. S9†); the reported H^+/Li^+ exchange in humid air[24] could be expected to block the Li-ion conduction pathway and hamper ionic conductivity. Similarly, Wang *et al.* also demonstrated the effect of H^+/Li^+ exchange on the ionic conductivity of LLZO compounds.[47] In their study, although the bulk resistances were first observed to drop for the samples tested at 150, 200 and 250 °C under moisture flow, the resistance values considerably deteriorated under prolonged exposure times that was linked to the blocking effect of protons.[47] CO_2 present in the atmosphere could also be expected to have a negative impact on ionic conductivity through the formation of Li_2CO_3 at grain boundaries, as shown by different research groups.[24,47,48]

In Table 1, we compare synthesis and sintering conditions, Li-ionic conductivities, activation energies and relative densities for Al and Ga doped LLZO compounds with the low temperature synthesized-processed cubic c-$Li_{6.4}Ga_{0.2}La_3Zr_2O_{12}$. Compared to the previously reported Al- and Ga-doped cubic

Published on 04 August 2015. Downloaded by MIT Library on 6/18/2019 3:37:10 PM.

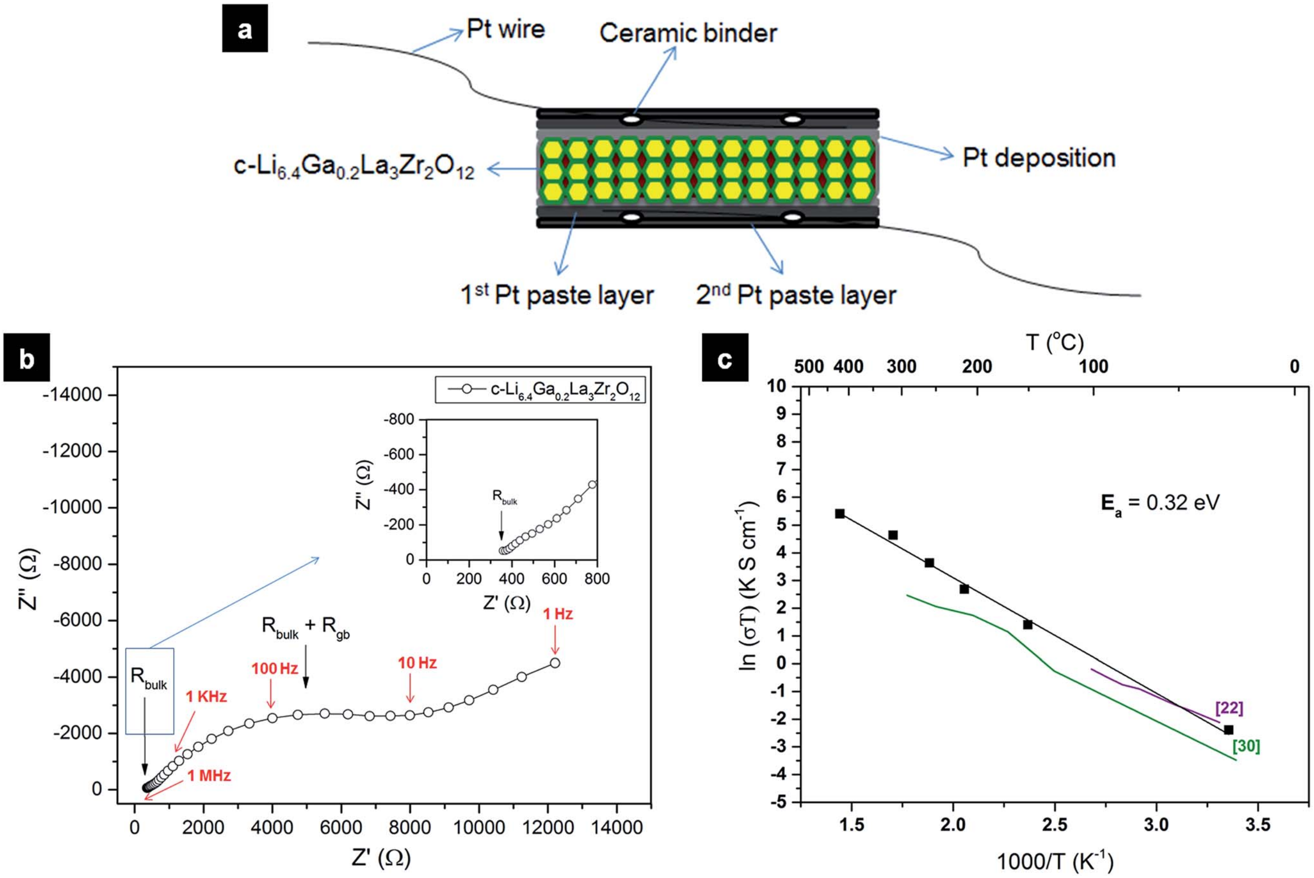

Fig. 5 (a) A typical pellet of cubic c-$Li_{6.4}Ga_{0.2}La_3Zr_2O_{12}$ with symmetric Pt electrodes and contacts used for AC electrochemical impedance analysis is presented schematically. (b) Nyquist plot of c-$Li_{6.4}Ga_{0.2}La_3Zr_2O_{12}$, obtained at room temperature (the measured pellet was sintered at 950 °C for 6 hours). Measurements with Pt electrodes were carried out from 1 MHz to 1 Hz. (c) Arrhenius plot for bulk ionic conductivity of c-$Li_{6.4}Ga_{0.2}La_3Zr_2O_{12}$. For comparison, ionic conductivities reported for Al[22] and Ga[30] doped cubic c-LLZO are also represented.

LLZO sintered pellets, we show that the newly synthesized c-$Li_{6.4}Ga_{0.2}La_3Zr_2O_{12}$ is characterized by the following features. Firstly, the temperature for the powder synthesis was lowered by almost 300 °C with a successful structural and homogeneous incorporation of Ga over the LLZO particles. This results in a strongly lowered particle size in the range of ~200–300 nm. Secondly, the sintering temperature to obtain acceptable pellet densities of ~76–80% was reduced to 950 °C. Besides, the pellets could also be sintered at higher temperatures above ~1000 °C for longer times to reach higher densities; however, this may result in Li-loss from the system, especially, if the pellets are not properly covered with the parent or Li-rich powders.

In order to test this hypothesis and effects of higher processing temperatures on the ionic conductivity and structure of c-$Li_{6.4}Ga_{0.2}La_3Zr_2O_{12}$, we also sintered the pellets (processed from Ga_2O_3 + t-$Li_7La_3Zr_2O_{12}$ mixture) at higher temperatures. The new pellets were sintered for 10 hours under synthetic air, as higher densities were demonstrated by Kilner *et al.*[33] *via* preventing the humidity exposure of pellets at higher sintering temperatures. Fig. 6c illustrates the change of relative density for the c-$Li_{6.4}Ga_{0.2}La_3Zr_2O_{12}$ pellets with sintering temperature, and the bulk ionic conductivity values obtained for each pellet are indicated. The pellet sintered at 1000 °C shows increased density ~86%, and a bulk ionic conductivity of 7.6×10^{-4} S cm^{-1} in the range of the low temperature sintered pellet. Interestingly, when the pellets are sintered at temperatures higher than 1000 °C, they lose weight and their density decreases indicating Li-loss from the system, Fig. 6b; *viz.* the relative density decreases to 69% and ionic conductivity drops to 0.6×10^{-4} S cm^{-1} for an increase of the sintering temperature to 1100 °C. In the latter pellet state, color changes and pit-like formations on the pellet surfaces are also clearly visible, see Fig. 6b. We turn to XRD powder diffraction and Raman spectroscopy to study the structural changes for the transition from relatively dense and highly conductive LLZO pellets to porous and one order of magnitude reduced conductive ceramics, Fig. 6a and d.

Up to 950 °C the sintered and dense pellets reveal a cubic c-$Li_{6.4}Ga_{0.2}La_3Zr_2O_{12}$ as originally obtained at 650 °C from the powder with comparable unit cell constants, see Fig. 6a and ESI Table S1 and S2.† However, we track important deviations in the XRD characteristics such as an increased higher background and broadening of the full width at half maximum diffraction peaks for the 1100 °C sintered lowest density pellets. In addition, the cubic cell constant is reduced to 12.958(4) Å (indexed

Published on 04 August 2015. Downloaded by MIT Library on 6/18/2019 3:37:10 PM.

Table 1 Literature overview of synthesis methods-conditions for the initial powders and sintering conditions to process solid Li-electrolyte pellets, the temperature indicating the main shrinkage as-observed in dilatometry, ionic conductivities at room temperature and corresponding activation energies (E_a), and relative densities achieved for the Li-site doped cubic Li-garnet compounds. We compare the state-of-the-art in the field with the newly suggested modified sol–gel combustion synthesis and post-Ga-doping processing route for cubic c-$Li_{6.4}Ga_{0.2}La_3Zr_2O_{12}$ electrolytes in this study

Compound	Synthesis conditions	Sintering conditions	Dilatometry[a]	Li-ion conductivity (S cm^{-1})	E_a (eV)	Relative density [%]	Ref.
$Li_7La_3Zr_2O_{12}$ (1.2 wt% Al)	Sol–gel 900, 1200 °C, 12 h	1200 °C/6 h (uniaxial)	~1150 °C	2.0×10^{-4}	n/a	86	25 and 46
$Li_{5.82}Al_{0.30}La_3Zr_{1.93}O_{11.72}$	Solid-state 1100 °C, 12 h	1100 °C/12 h	~1100 °C	2.3×10^{-4}	0.37	94	26
$Li_7La_3Zr_2O_{12}$	Solution method 750 °C, 8 h	750 °C/4 h	n/a	2.85×10^{-6}	0.36	89	37
$Li_{6.24}Al_{0.24}La_3Zr_2O_{11.98}$	Solid-state 1000 °C, 4 h	1000 °C/5 h (hot press)	n/a	4.0×10^{-4}	0.26	98	22
$Li_{6.55}Al_{0.15}La_3Zr_2O_{12}$	Spray pyrolysis 900–1000 °C, 1 h	1000 °C/1 h (uniaxial)	n/a	4.4×10^{-6}	0.49	51	23
$Li_{5.5}Ga_{0.5}La_3Zr_2O_{12}$	Solid-state 900 °C, 12 h	1150 °C/3 h	n/a	1.0×10^{-4}	n/a	80	30
$Li_{6.4}Ga_{0.2}La_3Zr_2O_{12}$	Sol–gel (Pechini) 800 °C, 12 h	1085 °C/6 h	n/a	9.0×10^{-4}	0.3	94	33
$Li_{6.25}Ga_{0.25}La_3Zr_2O_{12}$	Co-precipitation, solid-state 1000 °C, 4 h	1000 °C/1 h (hot press)	n/a	3.5×10^{-4}	n/a	91	31
$Li_{7.8}La_3Zr_2O_{12+\delta}$ (1.0 Ga per one mole)	Sol–gel 1085 °C, 6 h	1085 °C/6 h (isostatic)	n/a	5.4×10^{-4}	0.32	93	32
$Li_{6.4}Ga_{0.2}La_3Zr_2O_{12}$	Modified sol–gel combustion 600–650 °C, 1–10 h	950 °C/6 h (isostatic)	~950 °C	4.0×10^{-4}	0.32	76	This work

[a] The temperature, at which the main sintering can be observed in dilatometry measurements.

with Werner's algorithm (TREOR)[44] and for LLZO (ICSD 182312 [18])), ESI Table S3.† Shoulder-like diffraction peaks next to the high intensity ones also appear, which cannot be related to any expected impurity phases, and these might be stemming from a fraction of cubic LLZO with slightly different cell parameters. These findings indicate that the pellet loses density and conductivity due to the partial amorphization with Li-loss in the ceramic, and also suggest potential rearrangements in the Li-sublattice of the LLZO.

To further elucidate the structural changes we acquired and investigated Raman spectra of the sintered cubic c-$Li_{6.4}Ga_{0.2}La_3Zr_2O_{12}$ pellets relative to the processing temperature at 950 °C and 1100 °C and also the initially synthesized powders of cubic c-$Li_{6.4}Ga_{0.2}La_3Zr_2O_{12}$ and tetragonal t-$Li_7La_3Zr_2O_{12}$ at 650 °C, see Fig. 6d. In a first attempt, we confirm the LLZO Raman near order characteristic and high phase purity of the synthesized powders through the alternative low temperature processing route described in this study (nano-c-$Li_{6.4}Ga_{0.2}La_3Zr_2O_{12}$ and t-$Li_7La_3Zr_2O_{12}$), which agree with other process-derived LLZO-materials in the literature.[24,29,49] Analyzing the Raman spectra of the powders as references, the low energy region <200–300 cm^{-1} and intermediate-energy region 300–550 cm^{-1} bands can be linked to translational modes of mobile cations and vibrational modes of LiO_4 and LaO_{12} in accordance with the literature, see ref. 24 and 49. Hence, there is a clear coupling to the Li–O sublattice which is detectable *via* Raman spectroscopy, and also the cubic and tetragonal phases can be assigned in accordance with the LLZO structures, Fig. 6c. Importantly, we demonstrate that for the low temperature sintered cubic c-$Li_{6.4}Ga_{0.2}La_3Zr_2O_{12}$ pellets at 950 °C similar Raman spectra to that acquired for the 650 °C powder cubic-reference can be obtained. These reveal broad peaks at around 254, 358 and 406 cm^{-1} from the intermediate energy region and two peaks at 103 and 116 cm^{-1} from the low energy region which confirm the vibrational modes of the Li–O and La–O sublattice bonding, which are in agreement with the literature.[24,49] However, a close Raman study of the low density and high temperature (1100 °C) sintered $Li_{6.4}Ga_{0.2}La_3Zr_2O_{12}$ pellets reveals additional vibrational modes as apparent shoulders at 98 and 123 cm^{-1} for the low energy bands and at 205, 282, 336 and 368 cm^{-1} for the intermediate energy bands which could be related to changes in the Li–O bonding sublattice. We interpret the emergence of new bands to the splitting of degenerate modes, and a potential overall reduction in the symmetry potentially indicating a structural rearrangement in the Li-sublattice of $Li_{6.4}Ga_{0.2}La_3Zr_2O_{12}$ with Li-loss. Ref. 49 reported that the general observation in Raman spectra of broadened peaks in the low energy region, as measured for the dense cubic Ga–LLZO-based pellets and powders, is related to the static or dynamic disorder of highly mobile Li^+-ions moving along the isotropic pathways connecting the different structure sites; once the Raman peaks sharpen and shoulders appear here such as in the given example of the low density and high

Published on 04 August 2015. Downloaded by MIT Library on 6/18/2019 3:37:10 PM.

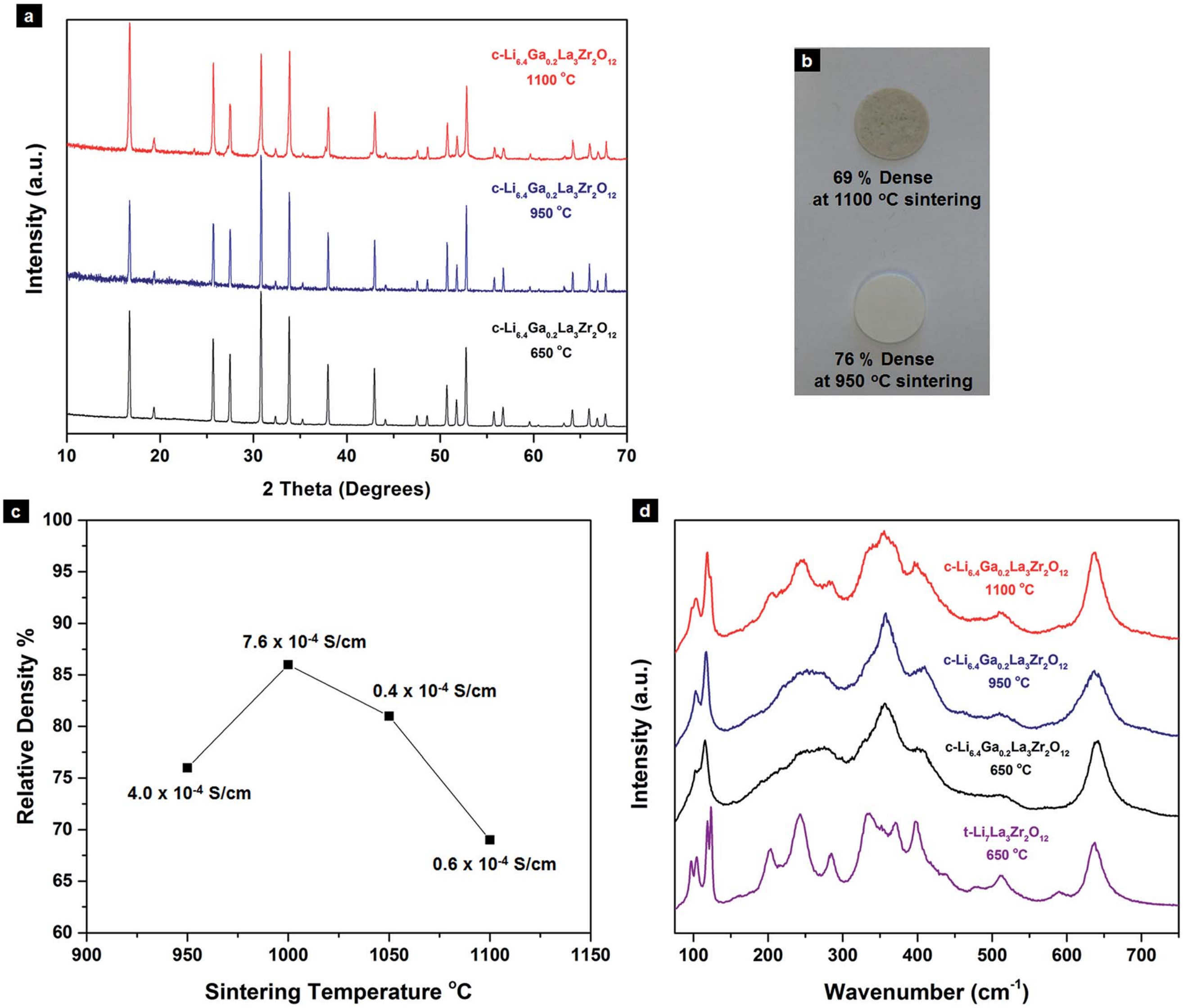

Fig. 6 (a) XRD powder patterns of c-$Li_{6.4}Ga_{0.2}La_3Zr_2O_{12}$: sample powder synthesized at 650 °C (black), pellet sintered at 950 °C for 6 hours (blue), pellet sintered at 1100 °C for 10 hours under synthetic air (red). (b) Typical pellets of c-$Li_{6.4}Ga_{0.2}La_3Zr_2O_{12}$ obtained after sintering at 950 °C for 6 hours (bottom) and at 1100 °C for 10 hours under synthetic air (top). (c) The change of relative density for the c-$Li_{6.4}Ga_{0.2}La_3Zr_2O_{12}$ pellets with sintering temperature. The bulk ionic conductivity values obtained for each pellet are indicated. (d) Raman spectra for t-$Li_7La_3Zr_2O_{12}$: sample powder synthesized at 650 °C (purple) and for c-$Li_{6.4}Ga_{0.2}La_3Zr_2O_{12}$: sample powder synthesized at 650 °C (black), pellet sintered at 950 °C for 6 hours (blue), pellet sintered at 1100 °C for 10 hours under synthetic air (red).

temperature sintered $Li_{6.4}Ga_{0.2}La_3Zr_2O_{12}$ in this study, the lattice distortion and Li-loss could be claimed leading to lower density and lower conduction.

To sum up, there is an optimum trade in Li-loss, sintering temperature and phase. We confirm high bulk Li-ion conductivities in the range of 4.0×10^{-4} S cm^{-1} for the low temperature synthesized-processed c-$Li_{6.4}Ga_{0.2}La_3Zr_2O_{12}$. Higher processing temperatures (~1100 °C) lead to Li-loss, substantial decrease in Li-ion conduction and in relative density, as well as to near order phase distortions.

In terms of ceramic processing, the implication of the lowered temperature processing and nanoparticle grained microstructure on the Li-ionic conductivity is striking. We report an equivalent Li-ionic conductivity when compared to other Ga-doped LLZO compounds processed at significantly higher temperatures. Usually, low ionic conductivities in the range of 10^{-6} S cm^{-1} with low pellet densities, *e.g.* 60%, are demonstrated for the low temperature synthesized and processed cubic $Li_7La_3Zr_2O_{12}$.[37,38] The improved properties here could be linked to the post-synthetic Ga-doping and the employment of nano-particles ensuring the proper densification of cubic LLZO pellets. Though Ga^{3+} ions on the Li sites could block the Li-ion conduction pathway, especially at higher concentrations,[33] the conductivity is still enhanced *via* the formation of vacancies and disordered Li-sites that is also necessary to stabilize the cubic phase. Suggested potential glass-like inter-granular Ga-rich phases can also contribute to continuous and fast ion conduction. For the assembly of all-solid state batteries, electrode–solid

This journal is © The Royal Society of Chemistry 2015

Published on 04 August 2015. Downloaded by MIT Library on 6/18/2019 3:37:10 PM.

electrolyte composites are usually employed in order to ensure good ionic conduction in electrodes (anode or cathode) and to optimize electrode–electrolyte interface resistance. Thus, the utilization of LLZO nano-particles could be quite important and beneficial to ensure a better contact between nano-electrode and electrolyte particles, when co-sintering, tape-casting methods and electrode–solid electrolyte composites are necessary and used to construct complete all-solid state battery cells. Here, the presented low temperature synthesis-processing opens new perspectives for all-solid state Li-battery processing based on garnets. It may be hypothesized that lowering the overall powder processing and sintering temperature was advantageous to avoid Li-losses, and an alternative strategy to stabilize the cubic phase and to achieve homogeneous Ga distribution over the nano-grains was presented.

4. Conclusion

In conclusion, we developed a novel low temperature synthesis-processing route for garnet-type fast Li-ionic conductors that are potential electrolytes for all-solid state batteries. We substantially decreased the particle size, revealed stable phases for the desired cubic Ga-doped Li-garnet structures, offered new insights into the role of Ga-diffusion in the evolution of the structures and phases, and concluded on sintering guidelines towards fast Li-ion conducting solid electrolytes.

Here, the tetragonal phase of $Li_7La_3Zr_2O_{12}$ was synthesized by a modified sol–gel – combustion method at a temperature of $\sim$600 °C, one of the lowest reported for garnet-type fast Li-ion conductors. Post-synthetic Ga-doping was shown to induce a phase transformation to the cubic phase at a very low temperature of $\sim$100 °C. The synthesis-processing route and the subsequent dilatometry and *in situ* XRD experiments were also suggested as model experiments to understand the role and effects of Ga-incorporation and diffusion on the tetragonal to cubic phase transformation. We demonstrate homogeneous distributions of Ga, La and Zr over the c-$Li_{6.4}Ga_{0.2}La_3Zr_2O_{12}$ nanoparticles by STEM studies. Due to the high sintering activity of c-$Li_{6.4}Ga_{0.2}La_3Zr_2O_{12}$ nanoparticles, processing temperatures were considerably decreased compared to the state-of-art. The small particle size of c-$Li_{6.4}Ga_{0.2}La_3Zr_2O_{12}$, in the range of $\sim$300 nm, is expected to bring about further advantages in terms of an enhanced solid electrolyte–electrode assembly for the construction of all-solid state batteries.

AC electrochemical impedance measurements revealed high bulk Li-ionic conductivities in the range of $\sim 4.0 \times 10^{-4}$ S cm^{-1} at 20 °C for the c-$Li_{6.4}Ga_{0.2}La_3Zr_2O_{12}$ pellets processed at a rather low temperature of 950 °C for 6 h. Similar values are only reachable through more complicated and laborious methods, also employing much higher processing temperatures, pressures and longer sintering times. Besides, the investigations on 1100 °C sintered pellets through Raman spectroscopy and XRD powder diffraction confirm the rearrangement in the garnet structure with Li-loss for higher sintering temperatures, which further supports the benefits of the novel low temperature synthesis-processing route for garnet-type fast Li-ionic conductors. Thus, we provide insights into the correlation of Li-loss, Li^+-conductivity, density and the (Raman) near order characteristics to further implicate on the best pellet processing conditions.

The new synthesis and processing route for garnet type fast Li-ion conductors is rather a simple "shortcut" and cost efficient in terms of strongly decreased annealing times and temperatures, but yet ensuring high Li-ion conductivities for battery electrolytes. Implication for all-solid state battery application is the option to employ nano-particles in tape-casting methods and to co-sinter through the nano-particle structure electrodes towards fast Li-ion transfer interfaces, which could enable the use of a broader range of electrode materials with potentially higher storage capacities.

Acknowledgements

The authors thank Competence Center Energy and Mobility (CCEM) and ALSTOM for funding of the projects: Proposal 911 "All Solid State Li-Ion Batteries based on New Ceramic Li-Ion Electrolytes" and SP-ESC-A 03-14, ETH Zürich Foundation "All Solid State Li^+ Batteries with high Thermal Operation Window", respectively. The authors also thank Jan van den Broek for his help in the characterization of pellets sintered at 1100 °C, and Sebastian Schweiger for the operation of the Raman microscope.

References

1 X. L. Ji, K. T. Lee and L. F. Nazar, *Nat. Mater.*, 2009, **8**, 500–506.

2 J. Schuster, G. He, B. Mandlmeier, T. Yim, K. T. Lee, T. Bein and L. F. Nazar, *Angew. Chem., Int. Ed.*, 2012, **51**, 3591–3595.

3 S. Afyon, M. Worle and R. Nesper, *Angew. Chem., Int. Ed.*, 2013, **52**, 12541–12544.

4 A. Perea, K. Zaghib and D. Belanger, *J. Mater. Chem. A*, 2015, **3**, 2776–2783.

5 S. Afyon, D. Kundu, A. J. Darbandi, H. Hahn, F. Krumeich and R. Nesper, *J. Mater. Chem. A*, 2014, **2**, 18946–18951.

6 S. Afyon, F. Krumeich, C. Mensing, A. Borgschulte and R. Nesper, *Sci. Rep-UK*, 2014, **4**, 7113.

7 D. B. Le, S. Passerini, J. Guo, J. Ressler, B. B. Owens and W. H. Smyrl, *J. Electrochem. Soc.*, 1996, **143**, 2099–2104.

8 P. L. Moss, R. Fu, G. Au, E. J. Plichta, Y. Xin and J. P. Zheng, *J. Power Sources*, 2003, **124**, 261–265.

9 D. Larcher and J. M. Tarascon, *Nat. Chem.*, 2015, **7**, 19–29.

10 J. F. M. Oudenhoven, L. Baggetto and P. H. L. Notten, *Adv. Energy Mater.*, 2011, **1**, 10–33.

11 L. Baggetto, H. C. M. Knoops, R. A. H. Niessen, W. M. M. Kessels and P. H. L. Notten, *J. Mater. Chem.*, 2010, **20**, 3703–3708.

12 J. H. Pikul, H. G. Zhang, J. Cho, P. V. Braun and W. P. King, *Nat. Commun.*, 2013, **4**, 1732.

13 A. Evans, A. Bieberle-Hutter, J. L. M. Rupp and L. J. Gauckler, *J. Power Sources*, 2009, **194**, 119–129.

14 V. Thangadurai, S. Narayanan and D. Pinzaru, *Chem. Soc. Rev.*, 2014, **43**, 4714–4727.

Published on 04 August 2015. Downloaded by MIT Library on 6/18/2019 3:37:10 PM.

15 J. B. Goodenough and K. S. Park, *J. Am. Chem. Soc.*, 2013, **135**, 1167–1176.

16 R. Murugan, V. Thangadurai and W. Weppner, *Angew. Chem., Int. Ed.*, 2007, **46**, 7778–7781.

17 J. Awaka, N. Kijima, H. Hayakawa and J. Akimoto, *J. Solid State Chem.*, 2009, **182**, 2046–2052.

18 J. Awaka, A. Takashima, K. Kataoka, N. Kijima, Y. Idemoto and J. Akimoto, *Chem. Lett.*, 2011, **40**, 60–62.

19 N. Bernstein, M. D. Johannes and K. Hoang, *Phys. Rev. Lett.*, 2012, **109**.

20 D. Rettenwander, P. Blaha, R. Laskowski, K. Schwarz, P. Bottke, M. Wilkening, C. A. Geiger and G. Amthauer, *Chem. Mater.*, 2014, **26**, 2617–2623.

21 C. A. Geiger, E. Alekseev, B. Lazic, M. Fisch, T. Armbruster, R. Langner, M. Fechtelkord, N. Kim, T. Pettke and W. Weppner, *Inorg. Chem.*, 2011, **50**, 1089–1097.

22 E. Rangasamy, J. Wolfenstine and J. Sakamoto, *Solid State Ionics*, 2012, **206**, 28–32.

23 R. Djenadic, M. Botros, C. Benel, O. Clemens, S. Indris, A. Choudhary, T. Bergfeldt and H. Hahn, *Solid State Ionics*, 2014, **263**, 49–56.

24 G. Larraz, A. Orera and M. L. Sanjuan, *J. Mater. Chem. A*, 2013, **1**, 11419–11428.

25 Y. Jin and P. McGinn, *J. Power Sources*, 2011, **196**, 8683–8687.

26 L. Cheng, J. S. Park, H. M. Hou, V. Zorba, G. Y. Chen, T. Richardson, J. Cabana, R. Russo and M. Doeff, *J. Mater. Chem. A*, 2014, **2**, 172–181.

27 J. L. Allen, J. Wolfenstine, E. Rangasamy and J. Sakamoto, *J. Power Sources*, 2012, **206**, 315–319.

28 S. Adams and R. P. Rao, *J. Mater. Chem.*, 2012, **22**, 1426–1434.

29 G. T. Hitz, E. D. Wachsman and V. Thangadurai, *J. Electrochem. Soc.*, 2013, **160**, A1248–A1255.

30 M. A. Howard, O. Clemens, E. Kendrick, K. S. Knight, D. C. Apperley, P. A. Anderson and P. R. Slater, *Dalton Trans.*, 2012, 12048–12053.

31 J. Wolfenstine, J. Ratchford, E. Rangasamy, J. Sakamoto and J. L. Allen, *Mater. Chem. Phys.*, 2012, **134**, 571–575.

32 H. El Shinawi and J. Janek, *J. Power Sources*, 2013, **225**, 13–19.

33 C. Bernuy-Lopez, W. Manalastas, J. M. L. del Amo, A. Aguadero, F. Aguesse and J. A. Kilner, *Chem. Mater.*, 2014, **26**, 3610–3617.

34 D. Rettenwander, C. A. Geiger, M. Tribus, P. Tropper and G. Amthauer, *Inorg. Chem.*, 2014, **53**, 6264–6269.

35 D. Rettenwander, J. Langer, W. Schmidt, C. Arrer, K. J. Harris, V. Terskikh, G. R. Goward, M. Wilkening and G. Amthauer, *Chem. Mater.*, 2015, **27**, 3135–3142.

36 J. Sakamoto, E. Rangasamy, H. Kim, Y. Kim and J. Wolfenstine, *Nanotechnology*, 2013, **24**, 424005.

37 H. Xie, Y. T. Li and J. B. Goodenough, *Mater. Res. Bull.*, 2012, **47**, 1229–1232.

38 S. Toda, K. Ishiguro, Y. Shimonishi, A. Hirano, Y. Takeda, O. Yamamoto and N. Imanishi, *Solid State Ionics*, 2013, **233**, 102–106.

39 *ZView Software*, D. Johnson, ed. S. Associates, Inc., Southern Pines, 2008.

40 P. Barpanda, T. Ye, S. C. Chung, Y. Yamada, S. Nishimura and A. Yamada, *J. Mater. Chem.*, 2012, **22**, 13455–13459.

41 S. Afyon, D. Kundu, F. Krumeich and R. Nesper, *J. Power Sources*, 2013, **224**, 145–151.

42 S. Afyon, C. Mensing, F. Krumeich and R. Nesper, *Solid State Ionics*, 2014, **256**, 103–108.

43 I. Kokal, M. Somer, P. H. L. Notten and H. T. Hintzen, *Solid State Ionics*, 2011, **185**, 42–46.

44 P. E. Werner, L. Eriksson and M. Westdahl, *J. Appl. Crystallogr.*, 1985, **18**, 367–370.

45 A. Mikkelsen, E. Hilner, J. N. Andersen, S. Ghatnekar-Nilsson, L. Montelius and A. A. Zakharov, *Nanotechnology*, 2009, **20**, 325304.

46 Y. Jin, in *Chemical and Biomolecular Engineering*, The University of Notre Dame, Notre Dame, 2013, p. 113.

47 Y. X. Wang and W. Lai, *J. Power Sources*, 2015, **275**, 612–620.

48 L. Cheng, E. J. Crumlin, W. Chen, R. Qiao, H. Hou, S. Franz Lux, V. Zorba, R. Russo, R. Kostecki, Z. Liu, K. Persson, W. Yang, J. Cabana, T. Richardson, G. Chen and M. Doeff, *Phys. Chem. Chem. Phys.*, 2014, **16**, 18294–18300.

49 F. Tietz, T. Wegener, M. T. Gerhards, M. Giarola and G. Mariotto, *Solid State Ionics*, 2013, **230**, 77–82.

This journal is © The Royal Society of Chemistry 2015